Efficient X-Ray Scintillators Based on Facile Solution Processed Zero-Dimensional Organic Manganese Bromide Hybrid Films

*Tarannuma Ferdous Manny, Tunde Blessed Shonde, He Liu, Md Sazedul Islam, Oluwadara Joshua Olasupo, Jarek Viera, Sahel Moslemi, Mohammad Khizr, Cianna Chung, J.S. Raaj Vellore Winfred, Luis M. Stand, Edwin F. Hilinski, Joseph Schlenoff, Biwu Ma**

Tarannuma Ferdous Manny, Tunde Blessed Shonde, He Liu, Md Sazedul Islam, Oluwadara Joshua Olasupo, Jarek Viera, Sahel Moslemi, Mohammad Khizr, Cianna Chung, J.S. Raaj Vellore Winfred, Luis M. Stand, Edwin F. Hilinski, Joseph Schlenoff, Biwu Ma
Department of Chemistry and Biochemistry, Florida State University, Tallahassee, FL 32306, USA.
E-mail: bma@fsu.edu

Luis M. Stand
Department of Nuclear Engineering, University of Tennessee, Knoxville, TN 37996, USA

Keywords: scintillators, zero-dimensional organic metal halide hybrids, solution processing, amorphous films, luminescence

Zero dimensional (0D) organic metal halide hybrids (OMHHs) have recently emerged as a new generation of scintillation materials, due to their high luminescence quantum efficiency, sensitivity, stability, and cost-effectiveness. While numerous 0D OMHH scintillators have been developed to date, most of them are based on solution grown single crystals that require time-consuming synthesis and are limited in size. Here, we report for the first-time high-performance X-ray scintillators based on facile solution processed 0D OMHH amorphous films. By reacting triphenyl(9-phenyl-9H-carbazol-3-yl) phosphonium bromide (TPPcarzBr) with manganese bromide ($MnBr_2$), 0D $(TPPcarz)_2MnBr_4$ amorphous films can be prepared via solution processing with mild thermal annealing, which exhibit green photoluminescence with an emission maximum around 517 nm and a photoluminescence quantum efficiency of around 87%. The X-ray scintillation of 0D $(TPPcarz)_2MnBr_4$ amorphous films is characterized to exhibit a light yield of 44,600 photon MeV^{-1} and an outstanding linearity with a low limit of detection of 32.42 $nGy_{air}s^{-1}$ over a wide range of X-ray dose rates. The versatile processability of 0D $(TPPcarz)_2MnBr_4$ is illustrated with remarkable recyclability, high cost-effectiveness and

scalability for large-scale production. By taking advantages of the amorphous nature of newly designed OMHHs, our approach opens up new opportunities for developing high-performance, solution-processable scintillators.

1. Introduction

Scintillators, materials that emit light when exposed to ionizing radiation, play a crucial role in a wide range of applications, including medical imaging, security screening, nuclear physics, and industrial testing[1-9]. Commercially available scintillators based on either inorganic crystals or organic compounds have been foundational in radiation detection and imaging for decades[10-14]. Inorganic scintillators are known for their high light yield and good energy resolution, while organic scintillators offer faster response times and flexibility in form. However, these conventional materials have many notable limitations. For instance, inorganic scintillators often suffer from slow response times and are sensitive to temperature and mechanical stress, while organic scintillators typically have lower light yield and poorer energy resolution[15-17]. These issues of conventional scintillation materials impede performance in advanced applications, prompting the need for new-generation materials[16]. Additionally, greater environmental stability, non-toxicity, and cost-effective production are sought for new-generation scintillators, making them more practical and sustainable for widespread use.

Recently, zero dimensional (0D) organic metal halide hybrids (OMHHs), an emerging class of luminescent materials, have received great attention with applications in a wide range of areas, from light emitting diodes to anti-counterfeiting and scintillation[18-24]. With organic cations and metal halide anions forming ionically bonded systems, 0D OMHHs have shown great potential as a new generation of scintillation materials, combining the merits of both inorganic and organic scintillators to exhibit high light yield, fast response times, improved energy resolution, environmental stability, and cost-effectiveness. Following our reports of efficient X-ray scintillators based on 0D $(C_{38}H_{34}P_2)MnBr_4$ and $(C_{36}H_{30}NP_2)_2SbCl_5$ in 2020[1, 25], a number of single crystalline 0D OMMHs based scintillators have been developed[26-38]. While excellent scintillation properties have been achieved for many 0D OMHHs, processing high performance large size scintillators based on 0D OMHHs remains challenging. First, growing 0D OMHH single crystals is time consuming and obtaining large size 0D OMHH single crystals is not trivial. Given that researchers can only produce single crystals of up to a few centimeters, it is unrealistic to create large scintillators solely based on 0D OMHH single crystals. Another approach to making large scintillators involves blending 0D OMHH powders with a polymer matrix[1, 9]. However, this method faces numerous issues and challenges, such as reduced light yield due to photon absorption and scattering, optical clarity issues from heterogeneity and nonuniformity, and mechanical instability from thermal mismatches and aging.

Here, we introduce a facile approach to producing large size scintillators based on 0D OMHHs by developing amorphous 0D OMHHs through low-temperature solution processing. By taking advantage of the rich chemistry of OMHHs, using a noncrystalline organic halide salt (triphenyl(9-phenyl-9H-carbazol-3-yl) phosphonium bromide (TPPcarzBr) to react with $MnBr_2$, amorphous 0D $(TPPcarz)_2MnBr_4$ films exhibited green photoluminescence with an emission maximum at 517 nm and a photoluminescence quantum efficiency (PLQE) of around 87%. The

X-ray scintillation of 0D $(TPPcarz)_2MnBr_4$ amorphous films is characterized to exhibit a light yield of 44,600 photon MeV^{-1} and an outstanding linearity with a low limit of detection of 32.42 $nGy_{air}s^{-1}$ in ambient conditions over a wide range of X-ray dose rates. Remarkable long-term stability is also observed for amorphous 0D $(TPPcarz)_2MnBr_4$ films under both ambient and continuous radiation exposure conditions. Moreover, the amorphous feature of 0D $(TPPcarz)_2MnBr_4$ enables exceptional processability, allowing them to be shaped into various forms on demand, and re-softened and re-shaped multiple times like thermoplastics.

2. Results and Discussions

Most 0D OMHHs developed to date are crystalline materials synthesized by reacting organic and metal halide salts in solutions. To obtain amorphous films based on 0D OMHHs, appropriate noncrystalline organic halide salts, instead of crystalline ones, were adapted to react with metal halides. For proof of concept, triphenyl(9-phenyl-9H-carbazol-3-yl) phosphonium bromide (TPPcarzBr) was reacted with $MnBr_2$ to form 0D $(TPPcarz)_2MnBr_4$, as shown in Figure 1a. Specifically, TPPcarzBr and $MnBr_2$ with a 2:1 molar ratio was dissolved in dimethylformamide (DMF) at room temperature to form a clear homogeneous solution with a molar concentration of ~3M. The solution was then drop-cast onto a baking sheet and heated on a hot plate at 100° C for 24 hours (Figure 1b). After the solvent evaporated, the resulting yellowish transparent film could be easily peeled off from the baking sheet (a video demonstrating this process is available in the supplementary section). The thickness of films could be well tuned by controlling the solution concentration and casting area. Attempts to prepare smooth films using the same method with tetraphenyphosphonium bromide (TPPBr) and $MnBr_2$ were unsuccessful, with only highly non-homogeneous crystalline films obtained (Figure S1). This is not surprising if we consider the highly crystalline nature of TPPBr and replacing one of the phenyl groups with bulky carbazole unit in TPPBr results in TPPcarzBr with significantly reduced crystallinity.

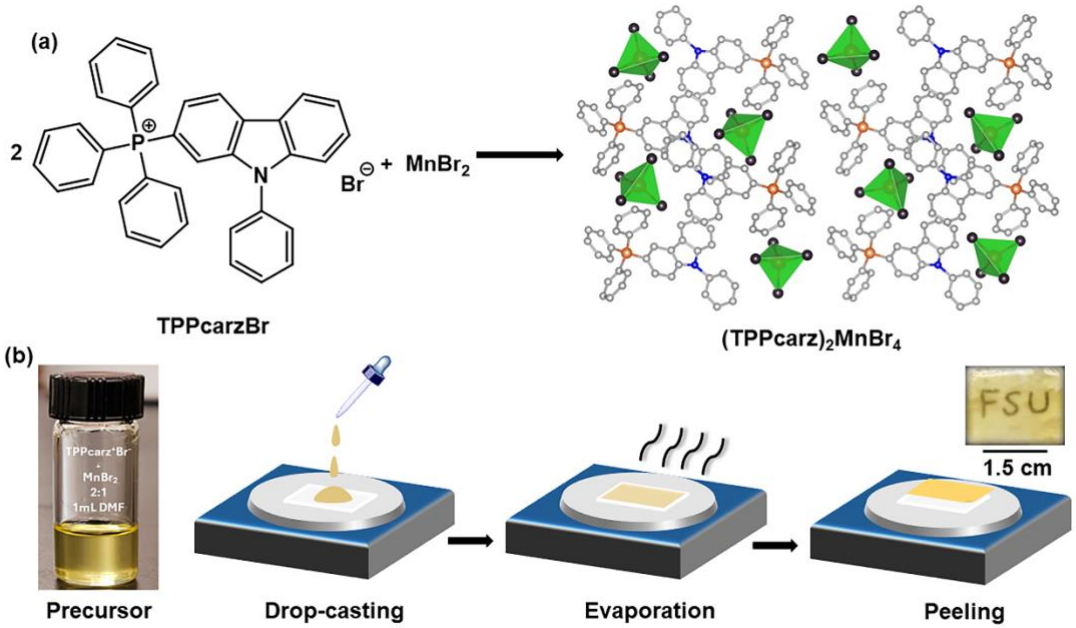

Figure 1. (a) Representation of the chemical reaction between TPPcarzBr and $MnBr_2$, and schematic structure of 0D $(TPPcarz)_2MnBr_4$, where tetrahedral $MnBr_4^{2-}$ anions are surrounded

and isolated by $TPPcarz^+$ cations (C, grey; N, blue; P, orange; Br, black ; Mn, light green; hydrogens are removed for clarity); (b) Scheme for the preparation of an amorphous $(TPPcarz)_2MnBr_4$ film via solution processing and thermal annealing.

To confirm the formation of 0D $(TPPcarz)_2MnBr_4$ amorphous films, we have characterized the compositional, structural, and optical properties of prepared films. Figure 2a shows a scanning electron microscopy (SEM) image of a prepared film with 1.5 cm length and 1.8 mm thickness as well the elemental mapping of various components, where a uniform spatial distribution of C, N, P, Mn, and Br elements is observed. The weight percent of each component matches well with the theoretical value of $(TPPcarz)_2MnBr_4$ (Figure S3), suggesting the formation of a product with the molar ratio of 2:1 for TPPcarz:$MnBr_4$. Powder X-ray diffraction (PXRD) was used to characterize the crystallinity of prepared films. Unlike clear diffraction patterns observed for crystalline $(TPP)_2MnBr_4$ (Figure S2), broadband patterns are observed for the $(TPPcarz)_2MnBr_4$ films (Figure 2b), suggesting an amorphous nature. The photophysical properties of films were thoroughly characterized using steady-state optical spectroscopy. Figure 2(c) shows the photoluminescence excitation (PLE) and emission (PL) spectra of films, which are almost identical to those of previously reported $(TPP)_2MnBr_4$ single crystals[1, 23]. The green emission (inset of Figure 2c) peaked at around 517 nm is attributed to the characteristic d-d transition of tetrahedral Mn(II) ($^4T_1 \rightarrow {}^6A_1$), which has a decay lifetime of around 392 µs (Figure S4) [1, 39]. All these results suggest the amorphous films are composed of 0D $(TPPcarz)_2MnBr_4$[39].

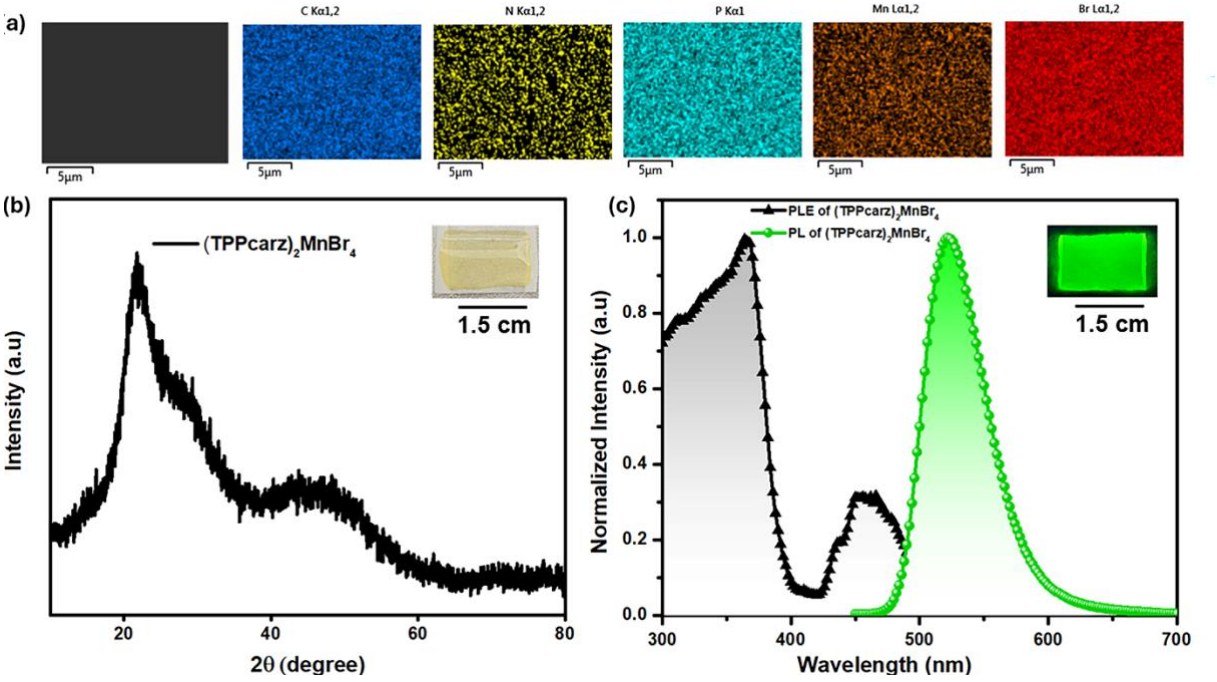

Figure 2. (a) Scanning electron microscopy (SEM) image of a solution-processed $(TPPcarz)_2MnBr_4$ film and corresponding elemental mapping of C, N, P, Mn, Br; (b) PXRD patterns of an amorphous $(TPPcarz)_2MnBr_4$ film (inset showing the image of the film under ambient light); (c) Excitation and emission spectra of an amorphous $(TPPcarz)_2MnBr_4$ film (inset showing the image of the film under UV light (365 nm)).

To evaluate the scintillation properties of 0D $(TPPcarz)_2MnBr_4$ amorphous films, the radioluminescence was first characterized. As shown in Figure 3a, green radioluminescence with an emission maximum at 517 nm is recorded under X-rays (~10.3 KeV), which is almost identical to the photoluminescence under UV light (365 nm). The radioluminescence intensity of 0D $(TPPcarz)_2MnBr_4$ amorphous films was also compared to that of $(TPP)_2MnBr_4$ single crystals (Figure S6). The minor difference in intensities suggests that 0D $(TPPcarz)_2MnBr_4$ amorphous films possess a similar light yield as that of $(TPP)_2MnBr_4$ single crystals. The radioluminescence of 0D $(TPPcarz)_2MnBr_4$ amorphous films shows an excellent linear dependence on the radiation dose rate in a wide range, as shown in Figure 3b. And the limit of detection is determined to be 32.42 $nGy_{air}s^{-1}$ by using the 3σ/slope method which is comparable to those of previously reported OMHHs[27, 40, 41], much lower than the X-ray diagnostic dose rate required for radiography (5.5 $\mu Gy_{air}\ s^{-1}$)[42]. The stability of 0D $(TPPcarz)_2MnBr_4$ amorphous films under continuous X-ray irradiation was also evaluated. It was found that the radioluminescence intensity of $(TPPcarz)_2MnBr_4$ remained unchanged after continuous irradiation for 5 days for 30 minutes each day (total dose was ~1992500μGy_{air}) and repeated 120 cycles on and off X-ray excitation (Figure 3c**)**. A video of the X-ray scintillation under continuous irradiation with a dose rate of 221.39 $\mu Gy_{air}s^{-1}$ can be found in the supplementary materials. To assess the potential of amorphous $(TPPcarz)_2MnBr_4$ based scintillators for practical X-ray imaging, a screen of 4 cm diameter size and 1.8 mm thickness was prepared (Figure 3d) and tested in a home-built X-ray imaging system (Figure S7) (See supplementary materials for the details of the setup). Figure 3e shows the X-ray image obtained for an opaque capsule with a built-in metallic spring, clearly demonstrating the suitability of 0D $(TPPcarz)_2MnBr_4$ amorphous films for X-ray radiography.

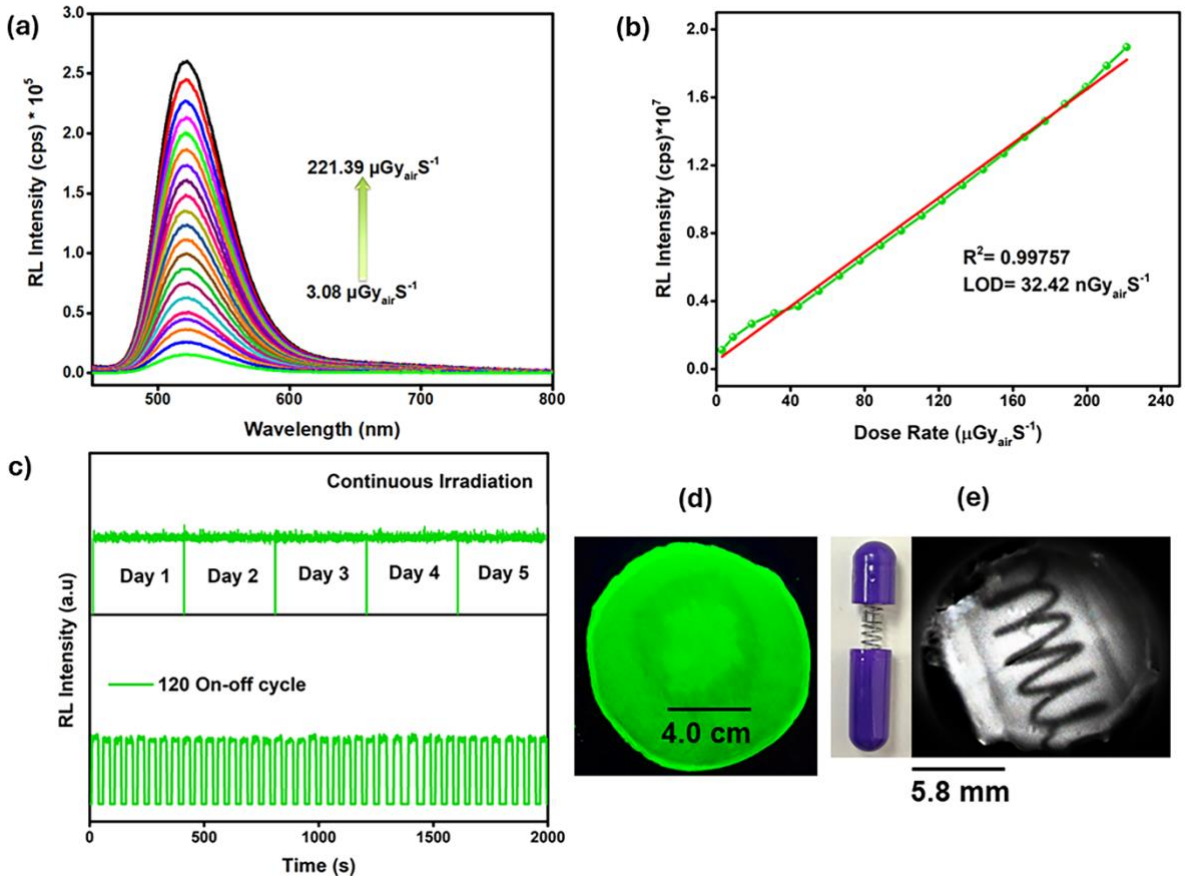

Figure 3. (a) Radioluminescence spectra of a 0D $(TPPcarz)_2MnBr_4$ amorphous film under X-ray excitation with dose rates ranging from 3.08 $\mu Gy_{air}s^{-1}$ 221.39 $\mu Gy_{air}s^{-1}$; (b) Dose rate dependence of the radioluminescence intensity of a 0D $(TPPcarz)_2MnBr_4$ amorphous film and the linear fitting with a limit of detection determined at 32.42 $nGy_{air}s^{-1}$; (c) The change of radioluminescence intensity of a 0D $(TPPcarz)_2MnBr_4$ amorphous film under continuous X-ray irradiation for 5 days and repeated on–off cycles at a dose rate of 221.39 $\mu Gy_{air}s^{-1}$, (d) A scintillator screen of 4 cm diameter size and 1.8 mm thickness prepared using our approach; (e) The X-ray image of an opaque capsule with a built-in metallic spring acquired with a digital camera, using 0D $(TPPcarz)_2MnBr_4$ amorphous film scintillator screen.

To further illustrate the merits of 0D $(TPPcarz)_2MnBr_4$ amorphous films, we have characterized the thermal and mechanical properties, as well as their versatile processability. Thermal stability is crucial for scintillators to ensure consistent performance across temperature variations. The thermal properties of $(TPPcarz)_2MnBr_4$ were investigated by thermogravimetric analysis (TGA) and differential scanning calorimetry (DSC). The melting point is measured at approximately 400°C, indicating high thermal stability. The DSC results confirm the amorphous nature of $(TPPcarz)_2MnBr_4$, as no sharp crystallization peak is observed during the exothermic heat flow in Figure 4a. Mechanical stability is another crucial attribute for scintillators as it ensures they maintain structural integrity and consistent performance under environmental stresses like temperature changes and physical impacts. Without mechanical stability, scintillators can develop defects that compromise efficiency and resolution, affecting the reliability of radiation detection. Compared to crystalline 0D OMHHs, amorphous ones are expected to have much better mechanical stability. Stress-strain measurement was performed on a 0D pellet shaped OMHH film with ~4.5 cm length and ~2.6 mm thickness to evaluate its mechanical response to applied stress, which provides insights into its elasticity, plasticity, and tensile strength. By incrementally increasing the stress and recording the resulting strain, a stress-strain curve was generated in Figure 4b. The elastic modulus and the elongation at break of the $(TPPcarz)_2MnBr_4$ film were measured to be 0.002 MPa and 6.7%, respectively. In contrast, single crystal $TPPMnBr_4$ is too hard and brittle to conduct the same stress-strain measurement. The superior mechanical resilience of amorphous $(TPPcarz)_2MnBr_4$ film compared to that of $TPPMnBr_4$ single crystal provides a clear advantage for its application in large size flexible scintillators that require certain tolerance against mechanical deformations.

$(TPPcarz)_2MnBr_4$ also exhibits excellent processability, as it can be softened and shaped into any desired shape using silicone molds (Figure 4c). Since the glass transition temperature is approximately 200°C, $(TPPcarz)_2MnBr_4$ can be softened by heating to this temperature. The softened material can then be poured into a preheated silicon mold with any shape. Upon cooling, the softened material can be shaped in a solid form. When reheated, the material can be resoftened, allowing it to be reshaped, thereby demonstrating its recyclability. Due to the excellent stability of $(TPPcarz)_2MnBr_4$, the optical and scintillation properties remain unchanged throughout these resoftening-reshaping processes. This versatile processing capability makes amorphous $(TPPcarz)_2MnBr_4$ ideal for application in scintillators requiring custom shapes and intricate designs. Its ease of reshaping reduces waste and enhances manufacturing efficiency, contributing to its appeal in practical uses.

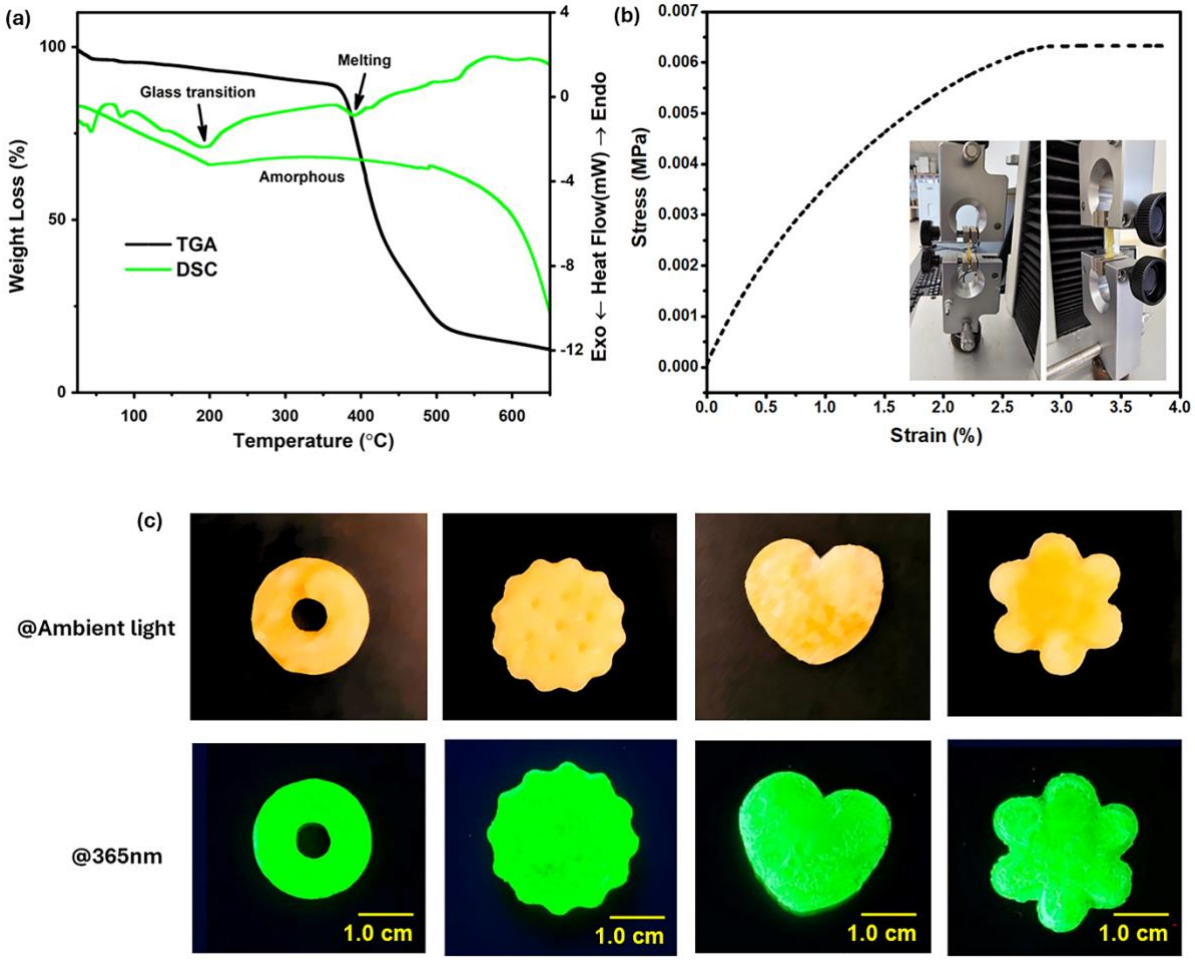

Figure 4. (a) TGA and DSC curves for $(TPPcarz)_2MnBr_4$. (b) The stress-strain characteristics of a 0D $(TPPcarz)_2MnBr_4$ amorphous film (the inset shows the mechanical testing setup, strain rate was 6 mm/min at RT); (c) The images of different shapes of amorphous $(TPPcarz)_2MnBr_4$ processed using molded resoftening-reshaping processes, under ambient and UV lights.

3. Conclusions

In summary, we have demonstrated the use of noncrystalline organic halide salts for the preparation of amorphous 0D organic metal halide hybrid films via simple low temperature solution processing. This processing method significantly simplifies the material manufacturing process, making it more cost-effective and scalable for large-scale production. The solution processed 0D $(TPPcarz)_2MnBr_4$ amorphous films exhibit green photoluminescence and radioluminescence with an emission maximum at 517 nm with a high photoluminescence quantum efficiency of ~87%, a radiation light yield of 44,600 photon MeV^{-1}, and an excellent linearity over a wide range of X-ray dose rates. In addition to excellent scintillation properties, solution processed amorphous $(TPPcarz)_2MnBr_4$ possesses high thermal stability, outstanding mechanical properties, and remarkable processability, making it a highly promising scintillation material for easy integration into various devices and systems with enhanced performance and sustainability. Our work underscores the remarkable versatility of 0D OMHHs, which can be

molecularly engineered to achieve desired functionalities for next-generation scintillators and numerous other applications.

4. Experimental section

Chemicals: Manganese(II) bromide, triphenylphosphine (TPP, 99%), 3-bromo-9-phenylcarbazole, nickel (II) Bromide, tetraphenylphosphonium Bromide (97%), diethyl ether (anhydrous), and dimethylformamide (DMF, anhydrous) were purchased from Sigma–Aldrich. Ethylene glycol was purchased from VWR. All reagents and solvents were used without further purification unless otherwise stated.

Synthesis of Triphenyl(9-Phenyl-9H-Carbazol-3-Yl)Phosphonium Bromide (TPPcarzBr): TPPcarzBr was synthesized following a previously reported method[43, 44]. In this synthesis, 524 mg (2 mmol) of triphenylphosphine, 644 mg (2 mmol) of 3-bromo-9-phenylcarbazole, and 50 mg (0.2 mmol) of $NiBr_2$ were added to 5 mL of ethylene glycol. The mixture was stirred at 150°C for 5 hours. The resulting deep green solution was dissolved in water and extracted with dichloromethane. The white powder product was then washed with diethyl ether, yielding a 95% recovery.

Preparation of $(TPPcarz)_2MnBr_4$ Film: 2 mmol of TPPcarzBr and 1 mmol of $MnBr_2$ were dissolved in 1mL of DMF until a completely clear precursor solution was obtained. Then the precursor solution was drop casted into baking paper and kept it in the hot plate at 100ºC for 24 hours.

Optical Characterization: Excitation and steady-state photoluminescence (PL) measurements were performed using an Edinburgh FS5 steady-state spectrometer equipped with a 150 W xenon lamp. The PLQE measurement was conducted using a Hamamatsu Quantaurus-QY Spectrometer (Model C11347-11), which includes a xenon lamp, an integrating sphere sample chamber, and a CCD detector. The PLQEs were calculated using the specified equation (Figure S5).

$$\eta_{QE} = \frac{I_S}{E_R - E_S} \qquad (1)$$

where I_s denotes the luminescence emission spectra of samples, E_R signifies the spectra of the excitation light for the reference (blank substrate), and E_s represents the excitation spectra for exciting the sample.

Powder XRD characterization: The powder X-ray diffraction (XRD) patterns were acquired using a Rigaku Smartlab powder diffractometer with a Cu Kα X-ray source. The diffraction data were collected over a 2θ range from 5° to 50° with a step size of 0.05°, under conditions of 44 mA tube current and 40 kV tube voltage at room temperature.

Radioluminescence characterization: The radioluminescence spectra were obtained using an Edinburgh FS5 spectrofluorometer (Edinburgh Instruments) outfitted with an X-ray source (Moxtek Mini-X tube featuring a tungsten (W) target and a maximum power output of 4 W). The radiation dose rate of the X-ray source was calibrated using a RaySafe 452 dosimeter. To determine the Limit of Detection (LOD), background signals were recorded under X-ray irradiation without the sample. Next, a series of signal responses was measured with the sample by incrementally increasing the X-ray dose rate, and the slope was calculated. The LOD was then derived using the equation provided below, with Bk_{std} representing the standard deviation of the background response.[45]

$$\frac{3*BK_{std}}{Slope} \qquad (2)$$

The light yield of $(TPPcarz)_2MnBr_4$ scintillator was estimated using the previously reported method[1], with Ce:LuAG serving as a reference (light yield of around 25,000 photon MeV^{-1}). The light yield was determined to be around 44,600 photon MeV^{-1}, similar to that of previously reported amorphous $(ETP)_2MnBr_4$.[26]

X-ray Imaging: The X-ray imaging system was constructed as illustrated in Figure S6. The imaging utilized a Moxtek Mini-X tube with a tungsten target and a maximum power output of 4 W. The dose rate applied was 221.39 $\mu Gy_{air}\ s^{-1}$. In this setup, the X-ray beam passed vertically through the object of interest, and the scintillator film was positioned directly beneath it. The radioluminescence generated was then deflected towards the camera by a reflector angled within the imaging system to mitigate the adverse effects of direct X-ray irradiation on the camera. A digital camera was used to capture the deflected image**.**

Elemental Characterization: The SEM Images and corresponding EDS spectrums of individual components were captured by Nova NanoSEM 400 (FEI Company) at 3.0 KV scanning voltage.

Thermal and DSC Analysis: Thermogravimetric analysis (TGA) was conducted using a TA Instruments Q600 system. The sample was heated from room temperature to 700°C at a rate of 5°C per minute under an argon flow of 100 mL per minute.

Tensile Testing: The mechanical testing of the amorphous film was done using Thümler GmbH tensile test machine Z3. A pellet sized film with ~4.5 cm length and ~2.6 mm thickness was prepared for testing the samples. The strain rate was 6 mm/min at room temperature. The Young's modulus is calculated using the Hook's Law from the initial, linear portion of the stress-strain curve, where the material behaves elastically.

$$E = \frac{\sigma}{\epsilon} \qquad (3)$$

Here, E is the Young's modulus, σ is the stress, and ϵ is the strain.

Strain is calculated using the formula:

$$\epsilon = \frac{\Delta L}{L_0} \qquad (4)$$

ϵ is the strain, ΔL is the change in length and L_0 is the original length.

Supporting Information

Supporting Information is available from the Wiley Online Library or from the author.

Conflicts of interest

T. F. M. and B. M. have filed an a provisional patent application "Organic Metal Halid Scintillators and Methods of Making" to the United States Patent and Trademark Office (Application # 63/677,463).

Acknowledgements

The authors thank the support from the National Science Foundation (DMR-2204466) and the FSU Office of Research. A portion of this research used resources provided by the X-ray Crystallography Center (FSU075000XRAY) and the Materials Characterization Laboratory (FSU075000MAC) at the FSU Department of Chemistry and Biochemistry.

Received: ((will be filled in by the editorial staff))

Revised: ((will be filled in by the editorial staff))

Published online: ((will be filled in by the editorial staff))

[1] L.-J. Xu, X. Lin, Q. He, M. Worku, B. Ma, *Nat. Commun.* **2020**, *11*, 4329.
[2] T. B. Shonde, M. Chaaban, H. Liu, O. J. Olasupo, A. Ben‐Akacha, F. G. Gonzalez, K. Julevich, X. Lin, J. R. V. Winfred, L. M. Stand, *Adv. Mater.* **2023**, *35*, 2301612.
[3] J. H. Heo, D. H. Shin, J. K. Park, D. H. Kim, S. J. Lee, S. H. Im, *Adv. Mater.* **2018**, *30*, 1801743.
[4] A. Jana, S. Cho, S. A. Patil, A. Meena, Y. Jo, V. G. Sree, Y. Park, H. Kim, H. Im, R. A. Taylor, *Mater. Today* **2022**, *55*, 110-136.
[5] H. Wu, Y. Ge, G. Niu, J. Tang, *Matter* **2021**, *4*, 144-163.
[6] Y. Zhou, J. Chen, O. M. Bakr, O. F. Mohammed, *ACS Energy Lett.* **2021**, *6*, 739-768.
[7] P. Lecoq, *Nuclear Instruments and Methods in Physics Research Section A: Accelerators, Spectrometers, Detectors and Associated Equipment* **2016**, *809*, 130-139.
[8] X. Ou, X. Chen, X. Xu, L. Xie, X. Chen, Z. Hong, H. Bai, X. Liu, Q. Chen, L. Li, *Research* **2021**.
[9] T. B. Shonde, A. Mondal, H. Liu, M. Chaaban, A. Ben-Akacha, S. Lee, E. S. Knorr, B. Ma, *ACS Mater. Lett.* **2022**, *4*, 271-276.
[10] F. Maddalena, L. Tjahjana, A. Xie, Arramel, S. Zeng, H. Wang, P. Coquet, W. Drozdowski, C. Dujardin, C. Dang, *Crystals* **2019**, *9*, 88.
[11] S. K. Gupta, Y. Mao, *Frontiers of Optoelectronics* **2020**, *13*, 156-187.
[12] S. Zhao, Z. Jia, Y. Huang, Q. Qian, Q. Lin, Z. Zang, *Adv. Funct. Mater.* **2023**, *33*, 2305858.
[13] T. Yanagida, *Proc. Jpn. Acad., Ser. B* **2018**, *94*, 75-97.
[14] W. Ma, Y. Su, Q. Zhang, C. Deng, L. Pasquali, W. Zhu, Y. Tian, P. Ran, Z. Chen, G. Yang, *Nat. Mater.* **2022**, *21*, 210-216.
[15] Q. Chen, J. Wu, X. Ou, B. Huang, J. Almutlaq, A. A. Zhumekenov, X. Guan, S. Han, L. Liang, Z. Yi, *Nature* **2018**, *561*, 88-93.
[16] C. Dujardin, E. Auffray, E. Bourret-Courchesne, P. Dorenbos, P. Lecoq, M. Nikl, A. Vasil'Ev, A. Yoshikawa, R.-Y. Zhu, *IEEE Trans. Nucl. Sci.* **2018**, *65*, 1977-1997.
[17] J.-X. Wang, L. Gutiérrez-Arzaluz, X. Wang, T. He, Y. Zhang, M. Eddaoudi, O. M. Bakr, O. F. Mohammed, *Nat. Photonics* **2022**, *16*, 869-875.
[18] C. Zhou, H. Lin, Y. Tian, Z. Yuan, R. Clark, B. Chen, L. J. van de Burgt, J. C. Wang, Y. Zhou, K. Hanson, *Chem. Sci.* **2018**, *9*, 586-593.
[19] L. Zhou, J. F. Liao, D. B. Kuang, *Adv. Opt. Mater.* **2021**, *9*, 2100544.
[20] C. Zhou, H. Lin, S. Lee, M. Chaaban, B. Ma, *Mater. Res. Lett.* **2018**, *6*, 552-569.
[21] M. Li, Z. Xia, *Chem. Soc. Rev.* **2021**, *50*, 2626-2662.
[22] E. Song, M. Chen, Z. Chen, Y. Zhou, W. Zhou, H.-T. Sun, X. Yang, J. Gan, S. Ye, Q. Zhang, *Nat. Commun.* **2022**, *13*, 2166.

[23] L. J. Xu, C. Z. Sun, H. Xiao, Y. Wu, Z. N. Chen, *Adv. Mater.* **2017**, *29*, 1605739.
[24] H. Liu, T. B. Shonde, F. Gonzalez, O. J. Olasupo, S. Lee, D. Luong, X. Lin, J. R. Vellore Winfred, E. Lochner, I. Fatima, *Adv. Mater.* **2023**, *35*, 2209417.
[25] Q. He, C. Zhou, L. Xu, S. Lee, X. Lin, J. Neu, M. Worku, M. Chaaban, B. Ma, *ACS Mater. Lett.* **2020**, *2*, 633-638.
[26] B. Li, Y. Xu, X. Zhang, K. Han, J. Jin, Z. Xia, *Adv. Opt. Mater.* **2022**, *10*, 2102793.
[27] Z.-Z. Zhang, J.-H. Wei, J.-B. Luo, X.-D. Wang, Z.-L. He, D.-B. Kuang, *ACS Appl. Mater. Interfaces* **2022**, *14*, 47913-47921.
[28] T. Xu, Y. Li, M. Nikl, R. Kucerkova, Z. Zhou, J. Chen, Y.-Y. Sun, G. Niu, J. Tang, Q. Wang, *ACS Appl. Mater. Interfaces* **2022**, *14*, 14157-14164.
[29] B. Su, J. Jin, Y. Peng, M. S. Molokeev, X. Yang, Z. Xia, *Adv. Opt. Mater.* **2022**, *10*, 2102619.
[30] J. Jin, K. Han, Y. Hu, Z. Xia, *Adv. Opt. Mater.* **2023**, *11*, 2300330.
[31] W. Shao, G. Zhu, X. Wang, Z. Zhang, H. Lv, W. Deng, X. Zhang, H. Liang, *ACS Appl. Mater. Interfaces* **2023**, *15*, 932-941.
[32] T. B. Shonde, H. Liu, O. J. Olasupo, A. Bouchard, S. Bouchard, A. Franklin, X. Lin, L. M. Stand, B. Ma, *Mater. Horiz.* **2024**.
[33] C. Sun, Z. Deng, Z. Li, Z. Chen, X. Zhang, J. Chen, H. Lu, P. Canepa, R. Chen, L. Mao, *Angew. Chem.* **2023**, *135*, e202216720.
[34] Y. Liu, Z. Xu, Z. Yang, Y. Zhang, J. Cui, Y. He, H. Ye, K. Zhao, H. Sun, R. Lu, *Matter* **2020**, *3*, 180-196.
[35] D. Liang, H. Xiao, W. Cai, S. Lu, S. Zhao, Z. Zang, L. Xie, *Adv. Opt. Mater.* **2023**, *11*, 2202997.
[36] S. B. Xiao, X. Zhang, X. Mao, H. J. Yang, Z. N. Chen, L. J. Xu, *Adv. Funct. Mater.* **2024**, 2404003.
[37] B. Li, J. Jin, M. Yin, K. Han, Y. Zhang, X. Zhang, A. Zhang, Z. Xia, Y. Xu, *Chem. Sci.* **2023**, *14*, 12238-12245.
[38] J. B. Luo, J. H. Wei, Z. Z. Zhang, Z. L. He, D. B. Kuang, *Angew. Chem.* **2023**, *135*, e202216504.
[39] V. Morad, I. Cherniukh, L. Pöttschacher, Y. Shynkarenko, S. Yakunin, M. V. Kovalenko, *Chem. Mater.* **2019**, *31*, 10161-10169.
[40] T. Jiang, W. Ma, H. Zhang, Y. Tian, G. Lin, W. Xiao, X. Yu, J. Qiu, X. Xu, Y. Yang, *Adv. Funct. Mater.* **2021**, *31*, 2009973.
[41] Z. Z. Zhang, Z. L. He, J. B. Luo, J. H. Wei, X. X. Guo, J. H. Chen, D. B. Kuang, *Adv. Opt. Mater.* **2024**, *12*, 2302434.
[42] H. Wei, Y. Fang, P. Mulligan, W. Chuirazzi, H.-H. Fang, C. Wang, B. R. Ecker, Y. Gao, M. A. Loi, L. Cao, *Nat. Photonics* **2016**, *10*, 333-339.
[43] L.-J. Xu, M. Worku, Q. He, H. Lin, C. Zhou, B. Chen, X. Lin, Y. Xin, B. Ma, *The Journal of Physical Chemistry Letters* **2019**, *10*, 5836-5840.
[44] H. Liu, T. B. Shonde, O. J. Olasupo, M. S. Islam, T. F. Manny, M. Woodhouse, X. Lin, J. R. Vellore Winfred, K. S. Mao, E. Lochner, *ACS Energy Lett.* **2023**, *8*, 4259-4266.
[45] X. Wang, H. Shi, H. Ma, W. Ye, L. Song, J. Zan, X. Yao, X. Ou, G. Yang, Z. Zhao, *Nat. Photonics* **2021**, *15*, 187-192.

X-ray scintillators based on amorphous organic manganese bromide hybrid films are demonstrated, which can be prepared via a facile solution processing with a noncrystalline organic bromide salt reacting with manganese bromide at low temperature. The solution processed scintillators exhibit excellent scintillation properties, thermal stability, mechanical resilience, and processability.

*Tarannuma Ferdous Manny, Tunde Blessed Shonde, He Liu, Md Sazedul Islam, Oluwadara Joshua Olasupo, Jarek Viera, Sahel Moslemi, Mohammad Khizr, Cianna Chung, J.S. Raaj Vellore Winfred, Luis M. Stand, Joseph Schlenoff, Edwin F. Hilinski, Biwu Ma**

Efficient X-Ray Scintillators Based on Facile Solution Processed Zero-Dimensional Organic Manganese Bromide Hybrid Films